


Photoluminescence-based detection of mechanical defects in multijunction solar cells

Cite as: J. Appl. Phys. **126**, 044503 (2019); <https://doi.org/10.1063/1.5106414>

Submitted: 28 April 2019 . Accepted: 14 June 2019 . Published Online: 23 July 2019

Claus G. Zimmermann 

COLLECTIONS

 This paper was selected as Featured



View Online



Export Citation



CrossMark

ARTICLES YOU MAY BE INTERESTED IN

[Organic photodetectors with frustrated charge transport for small-pitch image sensors](#)

Journal of Applied Physics **126**, 045501 (2019); <https://doi.org/10.1063/1.5102179>

[Measurement of spin mixing conductance in \$\text{Ni}_{81}\text{Fe}_{19}/\alpha\text{-W}\$ and \$\text{Ni}_{81}\text{Fe}_{19}/\beta\text{-W}\$ heterostructures via ferromagnetic resonance](#)

Journal of Applied Physics **126**, 043902 (2019); <https://doi.org/10.1063/1.5099913>

[Characterization of the electromechanical properties of \$\text{YCa}_4\text{O}\(\text{BO}_3\)_3\$ single crystals up to 800 °C](#)

Journal of Applied Physics **126**, 045104 (2019); <https://doi.org/10.1063/1.5093102>

Journal of
Applied Physics

SPECIAL TOPIC:
Polymer-Grafted Nanoparticles

Submit Today!

AIP
Publishing

Photoluminescence-based detection of mechanical defects in multijunction solar cells



Cite as: J. Appl. Phys. 126, 044503 (2019); doi: 10.1063/1.5106414

Submitted: 28 April 2019 · Accepted: 14 June 2019 ·

Published Online: 23 July 2019



Claus G. Zimmermann^{a)}

AFFILIATIONS

Airbus DS, 81663 Munich, Germany

^{a)}Electronic mail: claus.zimmermann@airbus.com

ABSTRACT

Mechanical solar cell defects give rise to a characteristic contrast in luminescence imaging. In multijunction cell architectures, the current in each subcell can be adjusted individually in photoluminescence imaging in contrast to electroluminescence imaging. The contrast formation under these conditions is derived theoretically. The image contrast of a defect recorded by illuminating and imaging one specific subcell can be reversed by illuminating the adjacent subcell in addition. This provides a convenient method to eliminate all background contrast by subtracting both images, resulting in an improved visibility of defects. This is demonstrated experimentally for the top cell of Ga_{0.5}In_{0.5}P/GaAs/Ge triple junction solar cells.

Published under license by AIP Publishing. <https://doi.org/10.1063/1.5106414>

I. INTRODUCTION

Cracks are an aspect of high practical relevance in the production of solar cells and modules, since they can negatively affect the cell performance as well as the reliability of the entire module. They are mechanical defects that are sometimes subdivided into microcracks, which are cracks completely internal to the cell, or macrocracks, which are running from one cell edge to another. Specifically microcracks, where the separation of the two cell areas is only in the range of some micrometers, are hard to detect solely visually. Therefore, several crack detection methods have been developed¹ for a single junction, monocrystalline or polycrystalline Si cells, which are the dominant cell types used terrestrially. The most predominant imaging techniques rely on lock-in thermography or luminescence imaging. In lock-in thermography, the infrared radiation emitted by the device is recorded, while the excitation can be performed by ultrasound,² current,³ or light.⁴ In luminescence techniques, charge carriers are either created by current injection resulting in electroluminescence⁵ (EL) or by monochromatic light. In this case, the recombination is termed photoluminescence (PL) and has found widespread use in Si solar cell production.^{6,7} One way of thinking about the contrast formation in EL or PL imaging is to treat the recombination occurring at the crack surface as a current sink. Due to the nonzero sheet resistance of the emitter and base, a gradual voltage drop toward the crack and consequently a decrease in the local pn junction voltage

will result. This reduces the luminescence emission⁸ and leads to a characteristic crack contrast.⁹

Also for III-V multijunction cells and modules, which are predominantly used for space applications, EL imaging is widely used for crack detection. PL imaging has been suggested, as well.¹⁰ The contrast formation in multijunction cells is more complex as compared to single junction cells, since the crack runs vertically through all subcells. Depending primarily on the different surface recombination velocities of the different subcell materials, current sinks of different magnitude are created. Electrically, all subcells are coupled and lateral currents can flow between the different subcells. Their magnitude and direction depend on the current sinks at the site of the crack. As an example, in Ga_{0.5}In_{0.5}P/GaAs/Ge triple junction cells, the GaAs middle cell has the largest surface recombination velocity, resulting in the dominant lateral current. This results in a typical dark crack feature in the EL luminescence image, while the contrast of the crack in the top cell luminescence image is reversed.⁹

Since in EL imaging the externally injected current is the same in all series connected subcells, there is no possibility to actively adjust the image contrast. In PL imaging, on the other hand, the (photo) current injected in each subcell can be adjusted arbitrarily by using subcell specific illumination. It is the purpose of this paper to show qualitatively that the tuneability of the photocurrent allows us to adjust the contrast of a cell crack in a wide range.

II. EXPERIMENT

As a test specimen, an $8 \times 4 \text{ cm}^2$ lattice matched $\text{Ga}_{0.5}\text{In}_{0.5}\text{P}/\text{GaAs}/\text{Ge}$ triple junction solar cell with a representative cell crack was used. For mechanical stability, the cell was bonded with silicone adhesive on an Al plate. Photoluminescence images under different illumination conditions were acquired with the help of a custom built setup. The cell on its Al support was placed on a temperature controlled vacuum chuck located inside a dark box designed to block all external light. For subcell specific illumination, three different light sources were installed. For excitation of the $\text{Ga}_{0.5}\text{In}_{0.5}\text{P}$ subcell, a 450 nm diode laser was used; for the GaAs middle cell, a 803 nm diode laser was used; and for the Ge bottom cell, a 975 nm diode laser was used. In front of each light source, a specially designed lens array ensured a homogeneous illumination of the whole cell area under the inclined illumination conditions. All three light sources were spatially aligned for a simultaneous illumination of all subcells. A calibration of the laser power settings vs photocurrent in the different subcells was performed with component cells representative for the triple junction solar cell technology used. The optical power of the three laser systems was sufficient to generate up to 3 times the photocurrent densities in the subcells generated under the AM0 space spectrum.

The luminescence images for top and middle cells were acquired with a Si CMOS camera with a 4 megapixel spatial resolution and a 1:20 000 dynamic range. Tailored dielectric filters in front of the camera lens ensured that only luminescence from the subcell of interest was detected and that scattered light from the excitation light sources was blocked. Imaging the bottom cell is fundamentally difficult due to the long wavelength of the emitted light and its low intensity which is a consequence of the indirect nature of the bandgap. This requires a low bandgap imaging sensor, which is only available in low resolution, and long exposure times, resulting in a poorer image quality compared to the other subcells. Therefore, the focus of this work was on recording top and middle cell images.

In Fig. 1, top cell photoluminescence images are illustrated, acquired with a constant photocurrent density of 17 mA/cm^2 , and simultaneous middle cell illumination varying from 0 to 30 mA/cm^2 . Without middle cell illumination, the cell crack is imaged as a dark line. Upon combining the top cell illumination with even a small simultaneous middle cell illumination around 3 mA/cm^2 , an inverted contrast starts to appear. Going to higher middle cell illumination levels enhances the bright contrast further. In Fig. 2, the same sequence of images is acquired for the middle cell. With a middle cell illumination of 7.2 mA/cm^2 and without any additional top cell illumination, the cell crack generates a fairly pronounced and broad contrast, which is indicative of a high surface recombination velocity. Upon simultaneous illumination of the top cell, the cell crack contrast becomes sharper. An inversion of the contrast comparable to the case of the top cell images, however, could not be observed, even at top cell illumination levels more than 6 times the middle cell level. The increased brightness in the left-hand part of the bottom image is the result of an inhomogeneous temperature distribution. The adhesive layer used to mount the cell on its Al support was applied nonuniformly and, in particular, did not extend up to the left cell edge. In combination

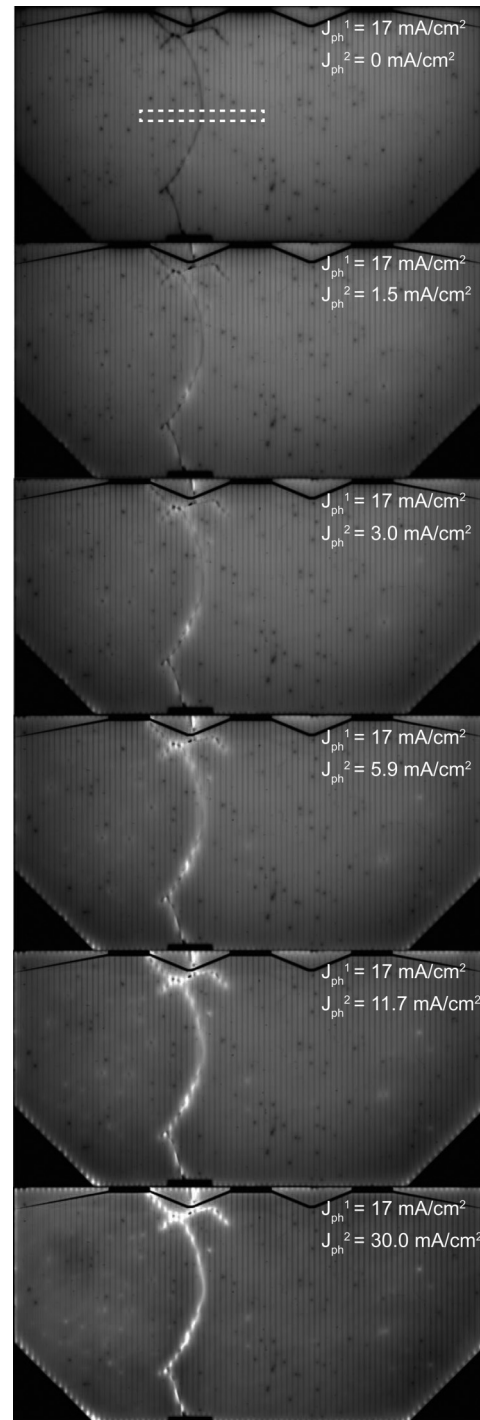


FIG. 1. Top cell photoluminescence images, acquired at a photocurrent density of 17 mA/cm^2 together with varying middle cell illumination levels. At a middle cell illumination of 3 mA/cm^2 , the contrast of the defect is inverted. The area chosen for a quantitative evaluation of the photoluminescence intensities is indicated.

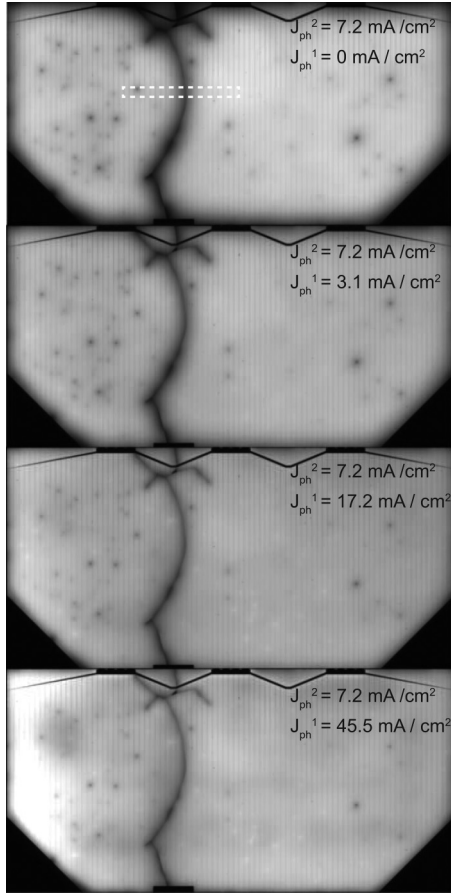


FIG. 2. Middle cell photoluminescence images, acquired at a photocurrent density of 7.2 mA/cm^2 together with varying top cell illumination levels. Even with a 6 times higher top cell illumination, contrast inversion cannot be achieved. The identical area as in Fig. 1 is chosen for a quantitative evaluation of the photoluminescence intensities.

with the high heat load introduced through the top cell illumination in this case, a spatially nonuniform temperature distribution resulted in the cell. The cell area on the left is, thus, running hotter and is forward biased by the remaining cell area due to its reduced open circuit voltage, resulting in an increased luminescence in this area.

III. THEORY

In order to model the contrast formation around a cell crack analytically, a one-dimensional network model as illustrated in Fig. 3 is considered. The cell crack is located at $x = 0$. The rear surface of the cell is fully metallized and, therefore, at a constant potential V . Since almost all triple junction cells are designed with an n on p polarity, the rearside potential equals the open circuit voltage V_{oc} of the cell. Similarly, the cell frontside is also modeled as an equipotential surface, which is at 0 V . Therefore, the effect of

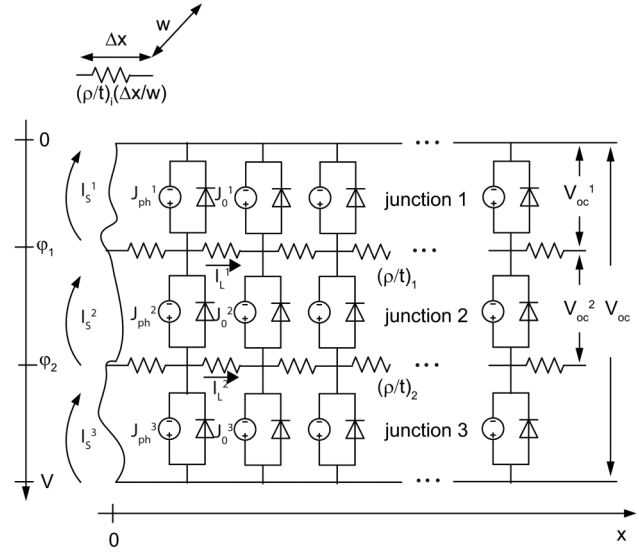


FIG. 3. Equivalent circuit diagram used to model the voltage distribution around a cell crack located at $x = 0$ for an n on the p triple junction solar cell. Currents are counted positive from higher to lower potentials as well as in the $+x$ direction.

individual gridfingers on the cell frontside is not taken into account. Top, middle, and bottom cells are referred to as junctions 1–3 in the following. The semiconductor layers between the pn junctions of layer 1 and layer 2, comprising among other layers, the base of junction 1, the tunnel junctions, and the emitter of junction 2, form a path for lateral current transport. The combined sheet resistance of this layer is denoted by $R_1 = (\rho/t)_1$. It is calculated as the ratio of the resistivity ρ and the thickness t of the individual semiconductor materials, taking the parallel nature of these current paths into account. The voltage distribution along this layer is given by $\phi_1(x)$. R_2 and $\phi_2(x)$ have the same meaning for the current transport path between layers 2 and 3. According to the generalized Planck equation,^{11–13} the amount of photons recombining radiatively in each junction i , $\Phi_i(x)$ is exponentially depending on the local junction voltage. In the case of junction 1, $\Phi_1(x)$ can be written as

$$\Phi_1(x) \propto \exp\left(\frac{e\phi_1(x)}{kT}\right), \quad (1)$$

where e , k , and T have their usual meaning. At a distance sufficiently far away from the crack, all junctions are at their respective open circuit voltage V_{oc}^i . By defining the voltage differences $v_1(x)$ and $v_2(x)$ according to

$$v_1(x) = \phi_1(x) - V_{oc}^1, \quad (2)$$

$$v_2(x) = \phi_2(x) - V_{oc}^1 - V_{oc}^2. \quad (3)$$

The change in luminescence contrast $\Delta\Phi_i(x)$ relative to the undisturbed luminescence intensity Φ_i^0 far away from the crack,

$\Delta\Phi_i(x) = \frac{\Phi_i(x) - \Phi_i^0}{\Phi_i^0}$, is given by

$$\Delta\Phi_1(x) = \frac{e}{kT} v_1(x), \quad (4a)$$

$$\Delta\Phi_2(x) = \frac{e}{kT} (v_2(x) - v_1(x)), \quad (4b)$$

$$\Delta\Phi_3(x) = -\frac{e}{kT} v_2(x). \quad (4c)$$

In Eq. (4), the simplification is made that the deviation in voltage from the respective open circuit voltage $v_i(x)$ is small compared to the thermal voltage, i.e., $v_i(x) < kT/e$, an assumption also made in the following to linearize equations. Since the maximum change $\Delta\Phi_i(0)$ in luminescence contrast amounts to $\approx \pm 50\%$ in Figs. 1 and 2, which is equivalent to a change in voltage of $0.7kT/e$, this assumption is not strictly fulfilled in all cases. It has been verified with the help of a circuit simulation tool that this simplification results in an uncertainty in the linearized luminescence profile of $\approx 20\%$, which is sufficient for a qualitative description.

In order to derive the luminescence image contrast of a cell crack according to Eq. (4), the local voltage distributions $\phi_1(x)$ and $\phi_2(x)$ have to be known. They can be determined by balancing the lateral current transport with the vertical current through each node according to Kirchhoff's law. The lateral current $I_L^i(x)$ in layer i is given by

$$I_L^i(x) = -\frac{w}{R_i} \frac{d\phi_i(x)}{dx}, \quad i = 1, 2, \quad (5)$$

where w denotes the arbitrary thickness of each node perpendicular to the plane of interest, as indicated in Fig. 3. The vertical current density J_v^i in each node is modeled by the simplified solar cell equation,

$$J_v^i(x) = J_0^i \exp\left(\frac{eV_i(x)}{n_i kT}\right) - J_{ph}^i, \quad i = 1-3, \quad (6)$$

with $V_1(x) = \phi_1(x)$, $V_2(x) = \phi_2(x) - \phi_1(x)$, and $V_3(x) = V_{oc} - \phi_2(x)$. The recombination current through the diode is characterized by the dark saturation current J_0^i and the ideality factor n_i . The external illumination gives rise to the photocurrent density J_{ph}^i . Applying Kirchhoff's law both at the intersection of junctions 1 and 2 as well as 2 and 3 and using the aforementioned simplification $v_i(x) < kT/e$ to linearize the exponential terms result in the following differential equations:

$$v_1'' = R_1[(a_1 + a_2)v_1 - a_2 v_2], \quad (7a)$$

$$v_2'' = R_2[-a_2 v_1 + [(a_2 + a_3)v_2], \quad (7b)$$

with

$$a_i = J_{ph}^i \frac{e}{n_i kT}, \quad (8)$$

where a_i can be interpreted as the slope of the I-V curve of junction i according to Eq. (6) at the open circuit voltage V_{oc}^i , which is essentially the inverse internal resistance of the voltage source each node represents. Introducing a matrix formalism, Eq. (7) can be

condensed into

$$\vec{v}'' = R\vec{v}, \quad (9)$$

with

$$\vec{v} = \begin{pmatrix} v_1 \\ v_2 \end{pmatrix}, \quad R = (r_{ij}),$$

$$\begin{aligned} r_{11} &= R_1(a_1 + a_2), \\ r_{12} &= -R_1 a_2, \\ r_{21} &= -R_2 a_2, \\ r_{22} &= R_2(a_2 + a_3). \end{aligned} \quad (10)$$

In order to solve Eq. (9), the appropriate boundary conditions have to be taken into account. One boundary condition is straightforward,

$$\vec{v}(x \rightarrow \infty) = \vec{0}, \quad (11)$$

which is equivalent to the statement that far away from the crack, all junctions are at their respective open circuit voltage. At the site of the crack $x = 0$, recombination takes place across the new semiconductor surface. The recombination current I_S^i across junction i is modeled as diodelike current with an ideality factor of 2,⁹

$$I_S^i = \frac{1}{2} w e S_i n_{int}^i (t_i^n + t_i^p) \exp\left(\frac{eV_i}{2kT}\right), \quad i = 1-3, \quad (12)$$

with $V_1 = \phi_1(0)$, $V_2 = \phi_2(0) - \phi_1(0)$, and $V_3 = V_{oc} - \phi_2(0)$. S_i denotes the surface recombination velocity, n_{int}^i is the intrinsic carrier concentration, and $t_i^n + t_i^p$ is the thickness of junction i . The lateral currents at $x = 0$ have to balance these recombination currents,

$$\begin{aligned} I_L^1(0) &= I_S^2 - I_S^1, \\ I_L^2(0) &= I_S^3 - I_S^2. \end{aligned} \quad (13)$$

Combining Eqs. (5), (12), and (13) and again linearizing the exponential term results in

$$\vec{v}'|_{x=0} = \vec{v}_0 + C\vec{v}(0), \quad (14)$$

with

$$\vec{v}_0 = \begin{pmatrix} R_1(K_1 - K_2) \\ R_2(K_2 - K_3) \end{pmatrix}, \quad C = (c_{ij}),$$

$$\begin{aligned} c_{11} &= \frac{e}{2kT} R_1(K_1 + K_2), \\ c_{12} &= -\frac{e}{2kT} R_1 K_2, \\ c_{21} &= -\frac{e}{2kT} R_2 K_2, \\ c_{22} &= \frac{e}{2kT} R_2(K_2 + K_3), \end{aligned} \quad (15)$$

and

$$K_i = \frac{1}{2} e S_i n_{int}^i (t_i^n + t_i^p) \left(\frac{J_{ph}^i}{J_0^i} \right)^{\frac{n_i}{2}}, \quad i = 1-3. \quad (16)$$

The coefficients K_i can be interpreted as the current dissipated per unit length at the site of the crack, in case all junctions would still be at their respective open circuit voltage at $x = 0$. The coefficients of matrices C and R exhibit the same structure in terms of the combination of the lateral resistances R_i with the coefficients a_i and K_i . Their magnitude can be directly adjusted by varying the illumination level of each subcell and thus J_{ph}^i .

The key step in solving Eq. (9) is to determine a matrix D which diagonalizes R such that

$$D^{-1} R D = R_d, \quad (17)$$

with

$$R_d = \begin{pmatrix} \lambda_1 & 0 \\ 0 & \lambda_2 \end{pmatrix}. \quad (18)$$

By substituting

$$\vec{z} = D^{-1} \vec{v}, \quad (19)$$

Eq. (9) becomes

$$\vec{z}'' = R_d \vec{z}. \quad (20)$$

The solution of this equation, taking the boundary condition according to Eq. (11) into account, is

$$\vec{z} = \vec{\alpha} \exp(-\sqrt{R_d} x), \quad \vec{\alpha} = \begin{pmatrix} \alpha_1 \\ \alpha_2 \end{pmatrix}. \quad (21)$$

The coefficient $\vec{\alpha}$ can be determined with the help of the second boundary condition according to Eq. (14) in combination with Eq. (19),

$$\vec{\alpha} = -(D\sqrt{R_d} + CD)^{-1} \vec{v}_0. \quad (22)$$

With $D = (d_{ij})$ and making use of Eqs. (18), (19), and (21), Eq. (4) can be expressed as

$$\Delta\Phi_1(x) = \frac{e}{kT} \left(d_{11}\alpha_1 e^{-\sqrt{\lambda_1}x} + d_{12}\alpha_2 e^{-\sqrt{\lambda_2}x} \right), \quad (23a)$$

$$\Delta\Phi_2(x) = \frac{e}{kT} (d_{21} - d_{11})\alpha_1 e^{-\sqrt{\lambda_1}x} + \frac{e}{kT} (d_{22} - d_{12})\alpha_2 e^{-\sqrt{\lambda_2}x}, \quad (23b)$$

$$\Delta\Phi_3(x) = -\frac{e}{kT} \left(d_{21}\alpha_1 e^{-\sqrt{\lambda_1}x} + d_{22}\alpha_2 e^{-\sqrt{\lambda_2}x} \right). \quad (23c)$$

For negative x values, Eq. (23) remains valid by replacing $-x$ by x . Diagonalizing the matrix R_d by determining D as well as the calculating of $\vec{\alpha}$ is quite involved in the most general case. For triple junction cells, the sheet resistances R_1 and R_2 are in the 100–1000 Ω range.¹⁴ In order to enable a more simplified solution, the approximation $R_1 \approx R_2 = R_0$ is made. As shown in the following, the experimentally measured luminescence images can be

reproduced using this simplification. The calculation of D and $\vec{\alpha}$ can be found in the Appendix.

IV. RESULTS AND DISCUSSION

For a qualitative analysis, the area highlighted by the rectangle in Figs. 1 and 2 has been chosen. It is oriented perpendicular to the crack and as such best suited for a one-dimensional analysis. The intensity Φ_1^0 far away from the crack has been used to normalize the luminescence intensities. In Figs. 4 and 5, the relative difference in intensity $\Delta\Phi_i(x) = \frac{\Phi_i(x) - \Phi_i^0}{\Phi_i^0}$ is plotted for the top ($i = 1$) and the middle cell ($i = 2$). Positive x values correspond to the right hand side of the crack in Figs. 1 and 2. In order to calculate the corresponding intensity profiles according to Eq. (23), the parameters summarized in Table I are required. The dark saturation currents J_0^i as well as diode ideality factors n_i were derived by fitting the light I-V curve of component cells of the same triple junction cell technology. The intrinsic carrier densities n_{int}^i only depend on the subcell materials and were chosen according to Ref. 15. Typical junction thicknesses $t_i^n + t_i^p$ for the chosen cell technology were used.

Included in the simulated curves is the effect of optical coupling. In high quality material, a significant fraction of the recombination is radiative. This emission can be absorbed by a lower bandgap subcell and results in an additional photocurrent there. For cells with an ideality factor close to one, the additional photocurrent in subcell j due to optical coupling, J_{ph-oc}^j , is directly proportional to the photocurrent J_{ph}^i in junction i above: $J_{ph-oc}^j = \eta_{ij} J_{ph}^i$. The proportionality constant η_{ij} is referred to as optical coupling coefficient. In the simulation, the additional

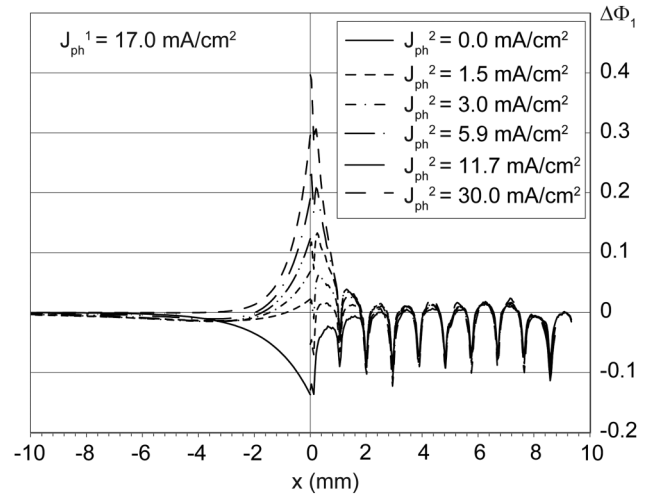


FIG. 4. Measured and simulated relative top cell photoluminescence intensities $\Delta\Phi_1(x) = \frac{\Phi_1(x) - \Phi_1^0}{\Phi_1^0}$ evaluated in the area indicated in Fig. 1. In order to improve readability, the symmetric nature of the intensity profile is used and the simulated curves are shown only for negative x values, whereas the measured profiles are only shown for positive x values. The oscillations in the measured curve are caused by the frontside grid.

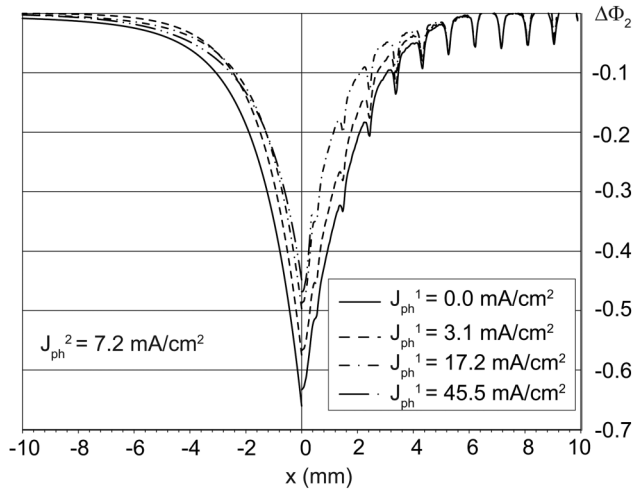


FIG. 5. Measured and simulated relative middle cell photoluminescence intensities $\Delta\Phi_2(x) = \frac{\Phi_2(x) - \Phi_2^0}{\Phi_2^0}$ evaluated in the area indicated in Fig. 2. Again, the simulated curves are shown for better readability only for negative x values, whereas the measured ones are plotted for positive x values.

current due to optical coupling is simply added to the externally induced photocurrent of junction j , J_{ph}^j .

The surface recombination velocities S_i , the sheet resistance R_0 , and the optical coupling coefficients η_{ij} were then adjusted to achieve the best fit to the experimental data. The resulting values are listed in Table I. It is important to note that the linearized model underestimates the real sheet resistance and surface recombination velocities by $\approx 20\%$ in this case. Nevertheless, it is possible to conclude that the chosen common sheet resistance R_0 is within the expected range.¹⁴ Similarly, the optical coupling constants are consistent with typical values for III-V cells,¹⁶ where the coupling from $\text{Ga}_{0.5}\text{In}_{0.5}\text{P}$ into GaAs is negligible, but significant from GaAs into Ge. The values of surface recombination velocities obtained are fully consistent with the ranges reported in the literature of $10\text{--}10^3$ cm/s for Ge,¹⁷ $10^5\text{--}10^6$ cm/s for GaAs,¹⁸ and $4\text{--}5 \times 10^4$ cm/s¹⁹ for $\text{Ga}_{0.5}\text{In}_{0.5}\text{P}$.

With these parameters, the simulated intensity profiles included in Figs. 4 and 5 reproduce the measured profiles well for

TABLE I. Numerical values used in the calculation. The parameters S_i , R_0 , and η_{ij} were adjusted to obtain the best fit to the measured intensity distributions in Figs. 4 and 5.

i	J_0^i (A/m ²)	n_i	n_{int}^i (cm ⁻³)	$t_i^n + t_i^p$ (μm)	S_i (cm/s)
1	5.6×10^{-20}	1.12	1.0×10^3	0.6	5.0×10^4
2	5.0×10^{-15}	1.03	2.1×10^6	1.5	2.5×10^5
3	2.1×10^{-2}	1	2.3×10^{13}	140	3.5×10^2
R_0 (Ω)	80				
η_{12}	0				
η_{23}	0.2				

all illumination levels, especially in the light of the simplifications made in the analytical model, most notably the linearization of the exponential terms and the use of one common sheet resistance value for R_1 and R_2 . The oscillations visible in the experimental curve are caused by the frontside grid, an effect that has not been included in the model. The contrast created in the top cell by a 17 mA/cm^2 illumination is reversed almost symmetrically by an additional middle cell illumination of $\approx 6\text{ mA/cm}^2$. The contrast created in the middle cell by a pure middle cell illumination of only 7.2 mA/cm^2 is much more pronounced and in addition much less affected by an additional top cell illumination. Even by a top cell illumination level 6 times higher than the one of the middle cell, contrast inversion cannot be achieved.

The behavior of the intensity profile in case of only top or only middle cell illumination can be readily understood. The analytical solution given in the Appendix is not applicable in these cases, since the inverse matrix cannot be calculated with the selected eigenvectors if only one subcell is illuminated. With the help of Eqs. (7), (11), and (14), the luminescence intensity profiles $\Delta\Phi_1(x)$ for the top cell illuminated case and $\Delta\Phi_2(x)$ for only middle cell illumination are derived as

$$\Delta\Phi_1(x) = -\frac{e}{kT} \frac{R_0 K_1 \exp(-\sqrt{R_0 a_1} x)}{\sqrt{R_0 a_1} + \frac{e}{2kT} R_0 K_1} \quad (24)$$

and

$$\Delta\Phi_2(x) = -\frac{e}{kT} \frac{2R_0 K_2 \exp(-\sqrt{2R_0 a_2} x)}{\sqrt{2R_0 a_2} + \frac{e}{2kT} 2R_0 K_2}. \quad (25)$$

For the given top cell illumination level of 17 mA/cm^2 and the cell parameters according to Table I, the coefficient K_1 , the current dissipated per unit length at the crack surface, equates to 0.033 A/m and the parameter a_1 to $5930\text{ 1}/\Omega\text{m}^2$. With these choices of parameters, the second term in the denominator of Eq. (24) can be neglected and the contrast at the site of the crack at $x = 0$ is $-e/kT \sqrt{R_0/a_1} K_1$. Therefore, the visibility of a crack in single subcell luminescence imaging depends linearly on K_1 and thus primarily on the surface recombination velocity S_1 according to Eq. (16). In addition, the magnitude of the luminescence contrast shows a square root dependence on the lateral sheet resistance R_0 . With a diode ideality factor close to 1, both K_1 and $\sqrt{a_1}$ exhibit the same $\sqrt{J_{ph}^1}$ dependence on the external illumination level according to Eqs. (8) and (16), which cancels out. Therefore, the magnitude of the luminescence contrast of a defect in single subcell illumination conditions is governed by the semiconductor properties surface recombination velocity and sheet resistance. They are determined by the device design but cannot be significantly altered by adjusting the external illumination.

The spatial variation away from the crack site shows an exponential dependence. As a characteristic parameter, the current spreading length $1/\sqrt{R_0 a_1}$ can be defined. It essentially characterizes the “sharpness” of a crack in the luminescence image and is inversely proportional to the square root of the product sheet resistance R_0 and inverse internal resistance a_1 of the top cell solar cell nodes. By increasing the external illumination J_{ph}^1 , a_1 increases and,

therefore, the current spreading length is reduced, resulting in a sharper image contrast.

According to Eq. (25), the middle cell luminescence contrast shows exactly the same functional dependence. Since the lateral current has to pass through the lateral layer between junctions 1 and 2 as well as through the same layer between junctions 2 and 3, the effective sheet resistance in this symmetrical case is $2R_0$. Due to this fact and, in particular, due to the almost one order of magnitude higher surface recombination velocity, the luminescence contrast is much more pronounced in this case compared to the top cell, as shown by the solid lines in Figs. 4 and 5.

The equations, given in the Appendix, for the triple junction case are quite complex to interpret for the case of the illumination of more than one subcell. It is, therefore, instructive to look at a simpler case of a tandem solar cell and to compare its behavior to the network model according to Fig. 3. The tandem cell network model is identical to the one illustrated in Fig. 3, with the omission of layer 3. There is only one lateral current path between layers 1 and 2 with sheet resistance R_0 , whereas $R_2 = 0$. The intensity profiles $\Delta\Phi_1(x)$ and $\Delta\Phi_2(x)$ for top and middle cells are derived as

$$\Delta\Phi_1(x) = -\frac{e R_0(K_1 - K_2) \exp(-\sqrt{R_0(a_1 + a_2)}x)}{kT \sqrt{R_0(a_1 + a_2)} + \frac{e}{2kT} R_0(K_1 + K_2)} \quad (26)$$

$$= -\Delta\Phi_2(x).$$

The resulting intensity profiles according to Eq. (26) are plotted in Fig. 6(a) for selected illumination conditions. Curve (i) shows the intensity profile for only top cell illumination (J_{ph}^1 [mA/cm²]/ J_{ph}^2 [mA/cm²]) of (17/0), and curve (ii) for pure middle cell illumination of (0/7.2). For a combined illumination of top and middle cells, the difference between the magnitude of the current dissipated at the crack surface in the top cell K_1 and in the middle cell K_2 determines whether the luminescence intensity at the crack site is increased in the top cell and decreased in the middle cell or vice versa.

For a typical illumination level of (17/7.2), K_1 amounts to 0.033 A/m and K_2 to 0.12 A/m. In this situation, in order to ensure current balance at the intersection of the crack with the lateral sheet resistance layer, the difference in current between K_1 and K_2 has to run laterally in the $+x$ direction away from the site of the crack. The associated voltage drop biases the individual top cell nodes forward, beyond their equilibrium open circuit voltage, such that they are consuming current. The lateral current is, thus, made up of two components, one feeding into the top cell nodes and a second one supplied by the middle cell nodes. Both current contributions flow in the $+x$ direction. For this reason, a_1 and a_2 parameters are additive in Eq. (26). For the top cell, the nodes close to the crack that were previously delivering current to the crack are now forward biased, consuming current as well. This additional current is delivered by top cell nodes far away from the crack. This implies that the boundary voltage V_{oc}^1 far away from the crack is slightly reduced by the additional illumination of the middle cell.

In line with the voltage distribution, the crack in the top cell shows a bright contrast and the one in the middle cell shows a dark one as shown by curve (iii) in Fig. 6(a). Although $K_2 \gg K_1$, the magnitude of the contrast in the middle cell is reduced

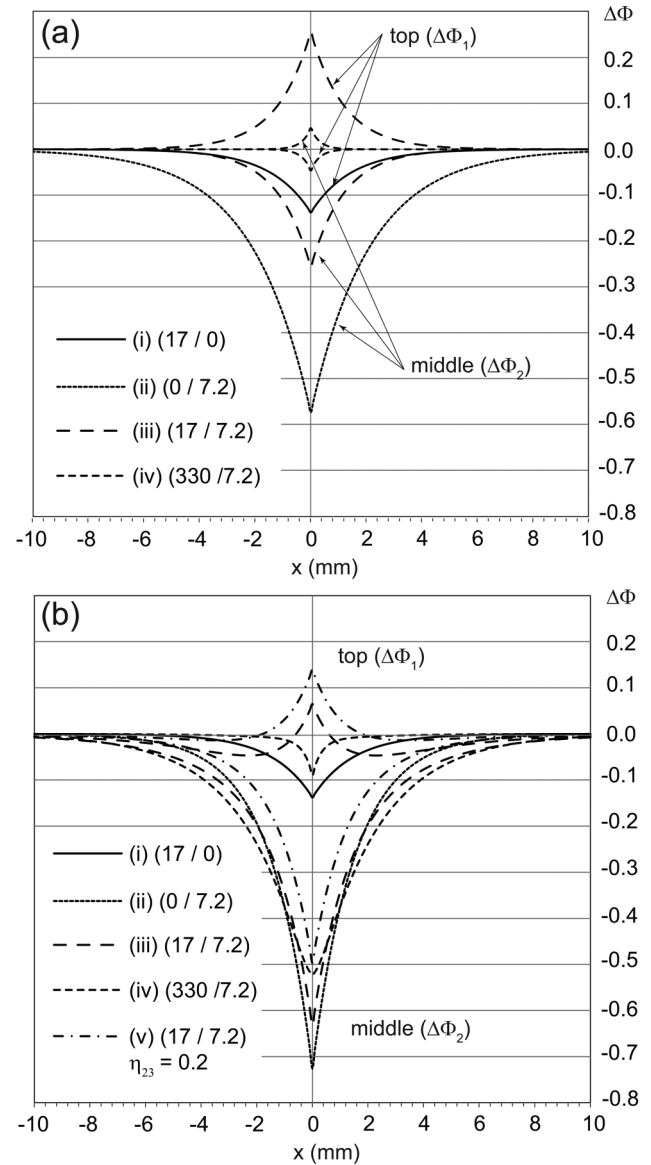


FIG. 6. Comparison of the top and middle cell luminescence intensity profiles $\Delta\Phi_1(x)$ and $\Delta\Phi_2(x)$ for selected illumination levels for (a) a simplified network model with $R_1 = R_0$ and $R_2 = 0$ and (b) the complete model with $R_1 = R_2 = R_0$.

nevertheless compared to the situation without simultaneous top cell illumination, since in the square root term in the denominator in Eq. (26), both parameters a_1 and a_2 contribute. The contrast in the top cell, however, is drastically affected: it is inverted and significantly increased compared to the pure top cell illumination due to the fact that in the nominator $K_2 - K_1$ is now much larger than K_1 in Eq. (24). Since the contributions from the top and middle cells are running along the lateral current path, the current spreading length $1/\sqrt{R_0(a_1 + a_2)}$ is reduced, leading to a sharper image contrast.

By increasing J_{ph}^1 by one order of magnitude to (170/7.2) $K_1 \approx K_2$ and no defect contrast is present anymore according to Eq. (26). By increasing J_{ph}^1 further, contrast inversion is achieved. This is shown in curve (iv) in Fig. 6(a) for an illumination level of (330/7.2). The current dissipated by K_1 cannot be supplied by K_2 alone and a lateral current toward the crack at $x = 0$ in the $-x$ direction is required to achieve current balance. In this situation, the top cell nodes are biased below their open circuit voltage and the current they deliver feeds into the lateral current. In addition, the voltage drop associated with the lateral current running in the $-x$ direction helps to forward bias the solar cell nodes in layer 2 above their open circuit voltage, and the current they are consuming runs again laterally in the $-x$ direction and constitutes a second contribution to the lateral current. In this case, the additional current consumed by the middle cell, compared to the situation without top cell illumination, has to be supplied by middle cell nodes far away from the crack, reducing V_{oc}^2 slightly.

The increase of J_{ph}^1 by two orders of magnitude changes the characteristic of the voltage sources represented by the individual top cell nodes. The slope of their I-V curve around their open circuit voltage is given by the parameter a_1 according to Eq. (8). $1/a_1$, thus, represents the internal resistance of these voltage sources. Since a_1 is directly proportional to J_{ph}^1 , increasing J_{ph}^1 lowers the internal resistance significantly and the top cell nodes start to resemble an ideal voltage source. Therefore, all excess current that is required to feed into the lateral layer can be delivered by a few top cell nodes close to the crack with only a small lateral voltage drop associated. As a consequence, both the current spreading length as well as the magnitude of the contrast at $x = 0$ become small according to Eq. (26).

An illumination condition of (330/7.2) is, in addition, a hypothetical case that can neither be achieved nor tolerated by the cell in practical operation. So, in the case of simultaneous illumination, it is again hard to work against an internally high surface recombination velocity, but the contrast of both subcells can be adjusted in a wide range nevertheless, unlike in the case of individual subcell illumination.

The behavior observed experimentally and described by the full network model with $R_1 = R_2 = R_0$ is quite different. The luminescence intensity profiles for the same illumination conditions as before are plotted in Fig. 6(b). For the single cell illumination condition, the top cell profile in curve (i) is identical, since exactly the same network model is used for this junction in both cases. Curve (ii) for pure middle cell illumination shows a more pronounced contrast, which is due to the fact that the effective series resistance is twice as high in this case with both current paths between layers 1/2 and 2/3 active, as pointed out before. For the combined (17/7.2) illumination case as shown by curve (iii), however, the situation is markedly different. Unlike in the simple model, the middle cell luminescence is hardly affected at all. Inversion in the top cell contrast is achieved, but significantly less pronounced than in curve (iii) in Fig. 6(a). Increasing the top cell illumination further to (330/7.2) again achieves a contrast reversal in the top cell, but again the contrast in the middle cell is only reduced slightly. The main difference between these two models, and thus the reason for the observed difference, is the lateral resistance path between layer 2/3.

In the case $K_1 > K_2$, there has to be a lateral current between layers 1 and 2 flowing in the $-x$ direction, with an associated voltage drop in the top cell, as observed. Identical to the situation discussed for the simple network model, the top cell nodes behave as ideal voltage sources, and therefore the current spreading length and the voltage drop associated with this lateral current in layer 1/2 are small. Unlike in the previous case, however, there is no equipotential surface on the rear side of layer 2 but the second lateral resistance path. The current associated with K_2 still has to run along this layer. The voltage sources in layer 2, however, have a much smaller a_2 parameter and, thus, a much higher internal resistance. Thus, to accommodate the complete current running in layer 2/3, a much larger voltage drop is required, associated with a much larger current spreading length. This results in a situation where the lateral current in layer 1/2 has subsided already at very small x values, but there is still a significant current in layer 2/3. The voltage drop ΔV associated with this current will be distributed between the top and middle cell nodes according to their internal resistance, i.e., $\Delta V_{top} = \Delta V a_1^{-1} / (a_1^{-1} + a_2^{-1}) \approx 0$ for the top cell and $\Delta V_{middle} = \Delta V a_2^{-1} / (a_1^{-1} + a_2^{-1}) \approx \Delta V$ for the middle cell. Therefore, the long range lateral current results in a voltage drop exclusively along the middle cell nodes and, therefore, to the strong luminescence contrast in the middle cell. The situation is, thus, close to a pure middle cell illumination scenario in which only one sheet resistance path of magnitude R_0 is active and in fact the intensity profile is close to case (ii) in Fig. 6(a).

While the middle cell contrast cannot be affected significantly in this scenario even by high top cell illumination, optical coupling, on the other hand, increases the tuneability of the image contrast again, as shown in curve (v). There the same illumination conditions of (17/7.2) as for curve (iii) are used, but with an optical coupling factor η_{23} of 0.2, resulting in an effective bottom cell illumination of 1.4 mA/cm^2 . This increases the contrast of the crack in the top cell markedly and decreases the one in the middle cell. Due to optical coupling, part of the current dissipated at the crack surface in layer 2 can directly be supplied by the bottom cell and flow along the equipotential rear side, without having to path through the lateral resistance between layers 2 and 3. Optical coupling between layers 2 and 3 can, therefore, be thought of as opening a "valve" for current flow through layer 3, thereby creating a situation closer to the simple network model.

In summary, the combination of high surface recombination velocity and significant sheet resistance paths between layer 2/3 severely limits the tuneability of the image contrast in the middle cell of $\text{Ga}_{0.5}\text{In}_{0.5}\text{P}/\text{GaAs}/\text{Ge}$ cells. For the top cell, on the other hand, the contrast can be adjusted in a wide range as illustrated in Fig. 4 by additional middle cell illumination. Nevertheless, $\approx 2 \text{ mm}$ away from the crack, the luminescence intensity reaches its constant equilibrium value under V_{oc} conditions. This tuneability of the image contrast provides an opportunity to enhance the defect contrast: The background image contrast can be removed by subtracting two top cell images with different illumination levels. In Fig. 7, the image without middle cell illumination has been subtracted from the image acquired with an additional middle cell illumination resulting in 11.7 mA/cm^2 photocurrent there.

As shown in Fig. 7, the contrast of the defect is greatly enhanced, while the background contrast has been removed. The

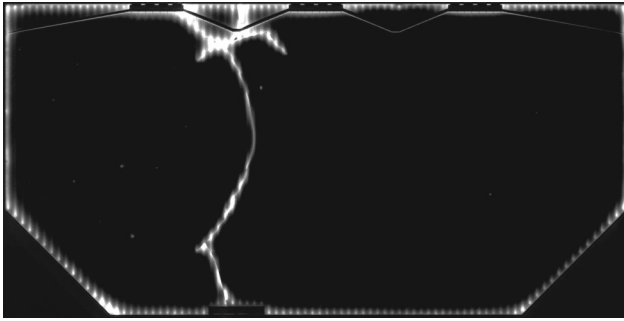


FIG. 7. Difference image obtained by subtracting a top cell luminescence image acquired with a photocurrent of 17 mA/cm^2 from the same image recorded with an additional middle cell illumination of 11.7 mA/cm^2 . The corresponding images can be found as the top image and the second image from the bottom in Fig. 1.

open pn junctions at the cell edge act as current sinks identical to the cell crack and create the bright image contrast around the cell circumference. Some local shunts can act electrically in an identical fashion as cell cracks, which explains the bright dots faintly visible in Fig. 7. By removing the background image contrast in this fashion, the resulting images lend themselves to simpler image processing algorithms aimed at detecting defects fully automatically. For standard electroluminescence or photoluminescence images, the varying background contrast still poses a challenge for defect detection algorithms.

Finally, it should be noted that the inversion of the contrast in the top cell through additional middle cell illumination implies that the top cell nodes close to the crack are biased beyond their intrinsic open circuit voltage and move from delivering current to the crack to consuming current. The additional current required is coming from top cell nodes far away from the crack which mandates that the externally measured open circuit voltage is slightly reduced, as pointed out earlier. Compared to the magnitude of the effect at the site of the crack, this effect on the overall top cell luminescence intensity is negligible. Likewise, large shunts in the cell epitaxy can be activated through additional middle cell illumination and the associated optical coupling to the bottom cell. The shunt is then connected to the grid system at the cell front and rearside and can affect the biasing condition of the entire cell slightly away from open circuit conditions compared to the pure top cell illumination case. For reasonable middle cell illumination levels of some mA/cm^2 , however, this does not cause a practical problem.

V. CONCLUSION

The magnitude of the contrast of a defect imaged by photoluminescence in single junction cells cannot be affected significantly by the external illumination conditions, except for a sharpening of the image contrast by increased illumination. For multijunction cells, however, the luminescence contrast of a mechanical cell defect can be adjusted in a wide range by simultaneous illumination of the junction imaged and its adjacent junction(s). This can then be conveniently exploited to subtract background contrast in the luminescence image by combining two images with a different contrast.

The range of tuneability is governed by the material parameters of the cell. The two most relevant parameters are the lateral sheet resistances R_i and the surface recombination velocities S_i . The optimum conditions in terms of contrast adjustment are given if the surface recombination velocities of the adjacent subcells are fairly similar, while the dominating lateral sheet resistance is located at the interface of the subcell imaged, and the adjacent cell that is illuminated in addition.

In case the surface recombination velocities of the different subcells are vastly different, the subcell most suitable for contrast inversion is the one with the lowest S_i . For this subcell, contrast inversion can always be achieved. To achieve contrast inversion for a subcell with a much higher surface recombination velocity faces both practical and principle difficulties. The photocurrent densities required in illuminating the adjacent subcell typically cannot be reached by the illumination sources. In addition, even if high current densities were to be achieved experimentally, the resulting short current spreading length results in a low contrast. If only one lateral current transport layer of significant resistance is present, a $\text{Ga}_{0.5}\text{In}_{0.5}\text{P}/\text{GaAs}$ dual junction cell is a good example for this scenario, contrast inversion could then be achieved nevertheless.

In case each subcell has its own lateral current transport path of significant resistance, the subcell with high S_i will always have a pronounced decrease in luminescence intensity at the site of the crack, which cannot be altered significantly by the illumination conditions of the subcell with low S_i .

A good method of increasing the range of contrast adjustability, primarily in the imaged subcell with the lower S_i , is illumination of one additional adjacent subcell, either directly through external illumination or indirectly through optical coupling. This can be beneficial, if, in this case, the resistance of one lateral transport path is effectively lowered. The Ge bottom cell in $\text{Ga}_{0.5}\text{In}_{0.5}\text{P}/\text{GaAs}/\text{Ge}$ triple junction cells is an example for this scenario.

APPENDIX: DERIVATION OF D , R_d , AND \vec{a}

In order to diagonalize R , the equation

$$\det(R - \lambda E) = 0 \quad (\text{A1})$$

has to be solved. E denotes the identity matrix. This results in the two eigenvalues λ_1 and λ_2 ,

$$\lambda_1 = \frac{r_{11} + r_{22}}{2} - \frac{1}{2} \sqrt{(r_{11} - r_{22})^2 + 4r_{12}r_{21}}, \quad (\text{A2a})$$

$$\lambda_2 = \frac{r_{11} + r_{22}}{2} + \frac{1}{2} \sqrt{(r_{11} - r_{22})^2 + 4r_{12}r_{21}}. \quad (\text{A2b})$$

Possible Eigenvectors \vec{e}_1 and \vec{e}_2 are

$$\vec{e}_1 = \begin{pmatrix} r_{12}/(\lambda_1 - r_{11}) \\ 1 \end{pmatrix}, \quad \vec{e}_2 = \begin{pmatrix} 1 \\ r_{21}/(\lambda_2 - r_{22}) \end{pmatrix}. \quad (\text{A3})$$

It is straightforward to show that $D = (\vec{e}_1 \quad \vec{e}_2)$ actually fulfills Eq. (17), i.e., that $D^{-1}RD = R_d$. The matrix D can be written as

$$D = \begin{pmatrix} \kappa & 1 \\ 1 & -\kappa \end{pmatrix} \quad (\text{A4})$$

with

$$\kappa = \frac{2r_{12}}{r_{22} - r_{11} - \sqrt{(r_{11} - r_{22})^2 + 4r_{12}^2}} \quad (\text{A5})$$

making use of the fact that $r_{12} = r_{21} = a_2 R_0$. The required coefficients d_{ij} in Eq. (23) are, thus, $d_{11} = -d_{22} = \kappa$, $d_{12} = d_{21} = 1$. The matrix $X = (D\sqrt{R_d} + CD)$ that has to be inverted to calculate $\tilde{\alpha}$ according to Eq. (22) is, therefore,

$$X = \begin{pmatrix} \kappa & 1 \\ 1 & -\kappa \end{pmatrix} \begin{pmatrix} \sqrt{\lambda_1} & 0 \\ 0 & \sqrt{\lambda_2} \end{pmatrix} + \frac{R_0 e}{2kT} \begin{pmatrix} K_1 + K_2 & -K_2 \\ -K_2 & K_2 + K_3 \end{pmatrix} \begin{pmatrix} \kappa & 1 \\ 1 & -\kappa \end{pmatrix}. \quad (\text{A6})$$

Determining the inverse matrix to X and multiplying it with $-\vec{v}_0$ yields $\tilde{\alpha}$ according to Eq. (22),

$$\alpha_1 = -\frac{R_0^2 e}{2kT \det X} \left(\frac{2kT}{R_0 e} \kappa (2K_2 K_3 - K_1 K_2 - K_1 K_3) - 2K_1 K_2 + K_1 K_3 + K_2 K_3 + \frac{2kT}{R_0 e} \sqrt{\lambda_2} (\kappa K_2 - \kappa K_1 + K_3 - K_2) \right), \quad (\text{A7})$$

$$\alpha_2 = -\frac{R_0^2 e}{2kT \det X} \left(\frac{2kT}{R_0 e} \kappa (2K_1 K_2 - K_1 K_3 - K_2 K_3) - K_1 K_2 + 2K_2 K_3 - K_1 K_3 + \frac{2kT}{R_0 e} \sqrt{\lambda_1} (-\kappa K_3 + \kappa K_2 + K_2 - K_1) \right), \quad (\text{A8})$$

with $\det X$ equating to

$$\det X = -\left(\frac{R_0 e}{2kT} \right)^2 (1 + \kappa^2) (K_1 K_2 + K_2 K_3 + K_1 K_3) - (1 + \kappa^2) \sqrt{\lambda_1 \lambda_2} - \frac{R_0 e}{2kT} \left((K_2 + K_3) (\kappa^2 \sqrt{\lambda_1} + \sqrt{\lambda_2}) + (K_1 + K_2) (\kappa^2 \sqrt{\lambda_2} + \sqrt{\lambda_1}) - 2K_2 \kappa (\sqrt{\lambda_2} - \sqrt{\lambda_1}) \right). \quad (\text{A9})$$

REFERENCES

- ¹M. Abdelhamid, R. Singh, and M. Omar, *IEEE J. Photovolt.* **4**, 514 (2014).
- ²J. Rakotoniaina, O. Breitenstein, M. Al Rifai, D. Franke, and A. Schnieder, in *Proceedings 19th European Photovoltaic Solar Energy Conference and Exhibition* (WIP, Munich, 2004), pp. 640–643.
- ³O. Breitenstein, J. Rakotoniaina, M. H. Al Rifai, and M. Werner, *Prog. Photovolt. Res. Appl.* **12**, 529 (2004).
- ⁴O. Breitenstein, J. Bauer, K. Bothe, D. Hinken, J. Müller, W. Kwapil, M. C. Schubert, and W. Warta, *IEEE J. Photovolt.* **1**, 159 (2011).
- ⁵T. Fuyuki, H. Kondo, T. Yamazaki, Y. Takahashi, and Y. Uraoka, *Appl. Phys. Lett.* **86**, 262108 (2005).
- ⁶T. Trupke, R. Bardos, M. Schubert, and W. Warta, *Appl. Phys. Lett.* **89**, 044107 (2006).
- ⁷M. Abbott, J. Cotter, F. Chen, T. Trupke, R. Bardos, and K. Fisher, *J. Appl. Phys.* **100**, 114514 (2006).
- ⁸U. Rau, *Phys. Rev. B* **76**, 085303 (2007).
- ⁹C. Zimmermann, *J. Appl. Phys.* **100**, 023714 (2006).
- ¹⁰Y. Kobayashi, M. Imaizumi, S. Kawakita, and M. Takahashi, JAXA Special Publication JAXA-SP-12-008E, 2012, Vol. 104.
- ¹¹W. van Roosbroeck, *Phys. Rev.* **94**, 1558 (1954).
- ¹²P. Würfel, *J. Phys. C Solid State Phys.* **15**, 3967 (1982).
- ¹³P. Würfel, S. Finkbeiner, and E. Daub, *Appl. Phys. A Mater. Sci. Process.* **60**, 67 (1995).
- ¹⁴H. Nesswetter, P. Lugli, A. W. Bett, and C. G. Zimmermann, in *2012 IEEE 38th Photovoltaic Specialists Conference (PVSC)* (IEEE, 2012), Vol. 2, pp. 1–6.
- ¹⁵S. R. Kurtz, D. Myers, and J. M. Olson, in *Conference Record of the Twenty-Sixth IEEE Photovoltaic Specialists Conference, 1997* (IEEE, 1997), pp. 875–878.
- ¹⁶H. Nesswetter, N. R. Jost, P. Lugli, A. W. Bett, and C. G. Zimmermann, *Prog. Photovolt. Res. Appl.* **24**, 760–773 (2015).
- ¹⁷D. Fitzgerald and A. Grove, *Surf. Sci.* **9**, 347 (1968).
- ¹⁸D. Aspnes, *Surfaces and Interfaces: Physics and Electronics* (Elsevier, 1983), pp. 406–421.
- ¹⁹S. Pearton, F. Ren, W. Hobson, C. Abernathy, R. Masaitis, and U. Chakrabarti, *Appl. Phys. Lett.* **63**, 3610 (1993).